X-ray observations of $2l$-nl' transitions in Mo^{30+}–Mo^{33+} from tokamak plasmas

J. E. Rice,[1] K. B. Fournier,[2] M. A. Graf,[1] J. L. Terry,[1]
M. Finkenthal,[3] F. Bombarda,[4] E. S. Marmar,[1] and W. H. Goldstein[2]
[1]*Plasma Fusion Center, Massachusetts Institute of Technology, Cambridge, Massachusetts 02139-4307*
[2]*Lawrence Livermore National Laboratory, Livermore, California 94550*
[3]*Johns Hopkins University, Baltimore, Maryland 21218*
[4]*Associazione ENEA–Euratom per la Fusione, 00044 Frascati, Italy*
(Received 9 January 1995)

X-ray spectra of $2p$-nd transitions with $4 \leq n \leq 18$ in molybdenum ($Z = 42$) charge states around neonlike (Mo^{32+}) have been observed from Alcator C-Mod plasmas. Accurate wavelengths (± 0.1 mÅ) have been determined by comparison with neighboring argon and chlorine lines with well-known wavelengths. Line identifications have been made by comparison to *ab initio* atomic-structure calculations, using a fully relativistic, parametric-potential code, and agreement between measured and theoretical wavelengths is good. Calculated wavelengths and oscillator strengths are presented for the strongest transitions with upper levels n between 4 and 14 to the lower levels $n = 2$ in the four charge states Mo^{30+}–Mo^{33+}. Effects of configuration interaction have been observed in the intensities of lines with nearly degenerate energy levels.

PACS number(s): 32.70.Fw, 32.30.Rj

INTRODUCTION

The soft-x-ray spectrum of molybdenum has been studied extensively in tokamak-, laser-, and pulsed-power-produced plasmas. In tokamaks, the abundance and spatial distribution of the various charge states affect the power balance of the plasma and may influence the current density profile, particle transport, and plasma resistivity [1,2]. In laser-produced plasmas, x-ray energy conversion efficiencies have been studied using molybdenum targets irradiated by high-power visible lasers [3]. These sources have also been used for emission spectroscopy studies of the 3-3, 2-2, 2-3, and 2-4 transitions of the charge states around the neonlike isosequence [4–7]. Theoretical energy level computations have been limited mainly to these transitions [8,9]. Transitions between highly excited states and ground or near-ground states have not been reported in the past. In high-density (laser and pulsed-power) plasmas, these levels may be depopulated by collisions; in high-temperature, low-density ($10^{20}/m^3$) tokamak plasmas such measurements are possible. Besides the purely spectroscopic interest in these transitions (line classifications and comparison with *ab initio* atomic structure calculations), these lines are good candidates to benchmark the collisional-radiative models used in power-loss estimates, because of their great temperature sensitivity.

In spite of the deleterious effect of large concentrations of high-Z materials on fusion plasmas, they will have to be used in the walls and various structural components of future fusion reactors. The Alcator C-Mod tokamak [10] has all molybdenum plasma facing components and one of the main thrusts of the present experiments on this device is the study of the impurity production and the screening of the core plasma by means of the divertor configuration [11]. This provides the opportunity for the detailed study of molybdenum charge states around the neonlike isosequence. The $\Delta n = 1$ x-ray transitions from these charge states have previously been studied in Alcator A [12] and Alcator C [13] plasmas. $\Delta n \geq 1$ transitions have been obtained from exploding wires [14], but the wavelength resolution was low.

In the present paper, high-resolution x-ray observations (2.90 Å $\leq \lambda \leq 3.84$ Å) of $2 \leq \Delta n \leq 16$ transitions from Mo^{30+}, Mo^{31+}, Mo^{32+}, and Mo^{33+} are presented. For these measurements, the plasma parameters were in the range of $1.2 \times 10^{20}/m^3 \leq n_{e0} \leq 2.0 \times 10^{20}/m^3$, and $1500\ eV \leq T_{e0} \leq 2300\ eV$.

INSTRUMENT DESCRIPTION AND CALIBRATION METHOD

The spectra presented here were recorded by a five-chord, independently spatially scannable, high-resolution x-ray spectrometer array [15]. Each von Hamos–type spectrometer consists of a variable entrance slit, a quartz crystal ($2d = 6.687$ Å), and a position-sensitive proportional counter detector. Each spectrometer has a resolving power of 4000, a 3-cm spatial resolution, and a wavelength range of 2.8–4.0 Å. Spectra are typically collected every 50 ms during a discharge, with 120 mÅ covered at any one wavelength setting. A typical value of the spectrometer luminosity function is $7 \times 10^{-13}\ m^2 sr$, calculated from the crystal reflectivity, spectrometer geometry, and Be window transmission. Wavelength calibration has been achieved by determining the instrumental dispersions from reference to argon and chlorine lines. The argon was introduced through a piezoelectric valve and chlorine is an intrinsic impurity from solvents used to clean vacuum components. Lines from hydrogenlike and heliumlike charge states are taken to have well-known wavelengths, either measured or calculated. The

1050-2947/95/51(5)/3551(9)/$06.00

TABLE I. Calibration lines from Ar^{16+} and Ar^{17+}

Transition	Wavelength (mÅ)	Ref.
$1s2p\ ^1P_1-2p^2\ ^1D_2$	3771.79	[16]
$1s2s\ ^3S_1-2s2p\ ^3P_2$	3761.06	[16]
$1s2s\ ^1S_0-2s2p\ ^1P_1$	3755.26	[16]
$1s\ ^1S_{1/2}-2p\ ^2P_{1/2}$	3736.52	[17]
$1s\ ^1S_{1/2}-2p\ ^2P_{3/2}$	3731.10	[17]
$1s^2\ ^1S_0-1s3p\ ^3P_1$	3369.61	[18]
$1s^2\ ^1S_0-1s3p\ ^1P_1$	3365.71	[19]
$1s^2\ ^1S_0-1s4p\ ^1P_1$	3199.77	[19]
$1s\ ^1S_{1/2}-3p\ ^2P_{1/2}$	3151.38	[17]
$1s\ ^1S_{1/2}-3p\ ^2P_{3/2}$	3150.24	[17]
$1s^2\ ^1S_0-1s5p\ ^1P_1$	3128.47	[20]
$1s^2\ ^1S_0-1s6p\ ^1P_1$	3090.91	[20]
$1s^2\ ^1S_0-1s7p\ ^1P_1$	3068.70	[20]
$1s^2\ ^1S_0-1s8p\ ^1P_1$	3054.43	[20]
$1s^2\ ^1S_0-1s9p\ ^1P_1$	3045.06	[20]
$1s^2\ ^1S_0-1s10p\ ^1P_1$	3037.51	[20]
$1s^2\ ^1S_0-1s11p\ ^1P_1$	3032.75	[20]
$1s^2\ ^1S_0-1s12p\ ^1P_1$	3028.90	[20]
$1s\ ^1S_{1/2}-4p\ ^2P_{3/2}$	2987.34	[17]
$1s\ ^1S_{1/2}-5p\ ^2P_{3/2}$	2917.50	[17]
$1s\ ^1S_{1/2}-6p\ ^2P_{3/2}$	2881.04	[17]

TABLE II. Calibration lines from Cl^{15+} and Cl^{16+}.

Transition	Wavelength (mÅ)	Ref.
$1s^2\ ^1S_0-1s3p\ ^1P_1$	3789.89	[19]
$1s^2\ ^1S_0-1s4p\ ^1P_1$	3603.56	[19]
$1s\ ^1S_{1/2}-3p\ ^2P_{1/2}$	3534.63	[17]
$1s\ ^1S_{1/2}-3p\ ^2P_{3/2}$	3533.49	[17]
$1s^2\ ^1S_0-1s5p\ ^1P_1$	3523.35	[19]
$1s\ ^1S_{1/2}-4p\ ^2P_{3/2}$	3350.71	[17]
$1s\ ^1S_{1/2}-5p\ ^2P_{3/2}$	3272.36	[17]

transitions used in the current wavelength calibration are listed in Tables I and II, along with the appropriate references [16–20].

CALCULATION OF ENERGY LEVELS AND OSCILLATOR STRENGTHS

Ab initio atomic structure calculations for Mo^{29+} through Mo^{33+} (ground states $2p^63s^23p$ to $2s^22p^5$, respectively) have been performed using the HULLAC package developed at the Hebrew University and Lawrence Livermore National Laboratories. The HULLAC package produces atomic wave functions using the parametric potential code RELAC [21,22]. The package includes ANGLAR, which uses the graphic angular recoupling program NJGRAF to generate fine-structure levels in a *j-j*-coupling scheme for a set of user-specified electron configurations [23]. RELAC then calculates energy levels and radiative transition probabilities.

This paper presents the results for newly identified *2s-np*, *2p-ns*, and *2p-nd* transitions in highly ionized molybdenum. The *2p-nd* transitions considered here are strongly split by the j value of the $2p$ hole in the ionic core. The resonance transitions with upper states containing a $2p_{1/2}$ hole are always at much shorter wavelengths than the corresponding transitions with a $2p_{3/2}$ hole. This can lead to significant configuration interaction when a $2p_{1/2}nd$ orbital is close in energy to a $2p_{3/2}n'd(n'>n)$ orbital. Interaction between the orbitals will affect both transition rates and transition wavelengths [24]. Table III demonstrates the wave-function mixing in Mo^{32+} for a case where the degeneracy in energy makes the configuration interaction very strong; the near degeneracy in energy of the $(2p^5)_{1/2}6d_{3/2}$ $J=1$ state and the $(2p^5)_{3/2}7d_{j'}$ $J=1$ states means that a significant amount of the $(2p^5)_{1/2}6d_{3/2}$ $J=1$ state's wave function is made from components of other configurations. A similar near degeneracy also exists for the $(2p^5)_{1/2}8d_{3/2}$ $J=1$ state and the $(2p^5)_{3/2}11d_{j'}$ $J=1$ states in Mo^{32+}. The wave-function mixings that result from these degeneracies have observable effects on transition strengths and are discussed below (see Table IV). Similar configuration-interaction effects are seen in Mo^{31+} between the $(2p^5)_{1/2}[3s^2]7d_{3/2}$ $J=1$ state and the $(2p^5)_{3/2}[3s^2]9d_{5/2}$ $J=1$ state, and in Mo^{31+} between the $(2p^5)_{1/2}[3s]8d_{3/2}J=\frac{3}{2}$ state and the $(2p^5)_{3/2}[3s]11d_{5/2}$ $J=\frac{3}{2}$ state (see Table V). The near-perfect degeneracy of the physical states in Mo^{30+} means that the effect of the configuration interaction is extremely strong; indeed, the physical states in question are made up of almost equal parts of the two *jj* configurations from which they originate.

Whereas the effect of the configuration interactions described above is mainly to shift transition wavelengths and redistribute oscillator strengths, a different type of configuration-interaction effect is seen in Mo^{33+}. In

TABLE III. The *j-j* wave function components (in percent) of the Mo^{32+} $2p^56d$ and $2p^57d$ $J=1$ physical states. The coincidental overlap of the $(2p^5)_{1/2}nd$ and the $(2p^5)_{3/2}n'd(n'>n)$ orbitals in energy leads to the configuration interaction. Physical states are named for the dominant *jj*-basis function in their makeup, the calculated energy value of each state is listed next to its name.

		Mo^{32+} $J=1$, odd parity wave function purities (RELAC) Pure *jj* configurations					
Physical states	Energy (eV)	$(2p^5)_{3/2}6d_{3/2}$	$(2p^5)_{1/2}6d_{3/2}$	$(2p^5)_{3/2}6d_{5/2}$	$(2p^5)_{3/2}7d_{3/2}$	$(2p^5)_{1/2}7d_{3/2}$	$(2p^5)_{3/2}7d_{5/2}$
$(2p^5)_{3/2}6d_{3/2}$	3836.4	89.06	0.0	10.91	0.0	0.0	0.0
$(2p^5)_{1/2}6d_{3/2}$	3947.1	0.0	82.52	0.02	5.85	0.01	11.36
$(2p^5)_{3/2}6d_{5/2}$	3837.8	10.92	0.01	88.90	0.0	0.0	0.03
$(2p^5)_{3/2}7d_{3/2}$	3950.6	0.0	5.85	0.0	90.53	0.0	3.56
$(2p^5)_{1/2}7d_{3/2}$	4059.0	0.0	0.01	0.0	0.0	99.91	0.01
$(2p^5)_{3/2}7d_{5/2}$	3948.4	0.00	11.33	0.03	6.99	0.01	81.43

Table VI, the line at 3269.7 mÅ has been identified as a $2s$-7p transition. However, the upper state for this transition is named $2s^2 2p^4 7p$ $J=\frac{3}{2}$, following the convention described above. The final state for this transition is the $2s2p^6$ $J=\frac{1}{2}$ second excited state of Mo^{33+}. The only way the $2s2p^6$-$2s^2 2p^4 7p$ decay takes place is that, in reality, there is a 3.8% admixture of the $2s2p^5 5d$ $J=\frac{3}{2}$ j-j-basis function in the $2s^2 2p^4 7p$ $J=\frac{3}{2}$ state. Thus only through a $2p$-$5d$ dipole decay does this formally forbidden transition take place.

EXPERIMENTAL MOLYBDENUM SPECTRA

Shown in Fig. 1 is a spectrum between 3.7 and 3.8 Å, obtained from a plasma with an electron temperature of 1800 eV and an electron density of $1.7\times10^{20}/m^3$. This shows the brightest molybdenum line that falls in the

TABLE IV. Mo^{32+} ($2p^6$ ground-state) resonance transitions. The column labeled "upper state" shows the occupancy of the two relativistic $2p$ orbitals and the occupied upper orbital. In the case of a $2s$-np transition, the numbers shown are the occupancy of the $2s$ orbital, the spectator electrons, and the occupied upper orbital. The $(2p^5)_{3/2}$-$nd_{5/2}$ series limit is at 2914.78 mÅ, and the $(2p^5)_{1/2}$-$nd_{3/2}$ series limit is at 2841.44 mÅ.

Transition	Obs. λ (mÅ)	Theor. λ (mÅ)	λ (mÅ)	g^*f	Upper state
$2p$-19d		2867.4		1.16×10^{-3}	$(2p-)(2p+)^4 19d-J=1$
$2p$-18d		2870.6		1.38×10^{-3}	$(2p-)(2p+)^4 18d-J=1$
$2p$-17d		2874.3		1.60×10^{-3}	$(2p-)(2p+)^4 17d-J=1$
$2p$-16d		2878.7		1.90×10^{-3}	$(2p-)(2p+)^4 16d-J=1$
$2p$-15d		2884.1		2.26×10^{-3}	$(2p-)(2p+)^4 15d-J=1$
$2p$-14d		2891.1		7.07×10^{-3}	$(2p-)(2p+)^4 14d-J=1$
$2p$-13d		2899.3		6.44×10^{-3}	$(2p-)(2p+)^4 13d-J=1$
$2p$-12d	2910.2	2909.8	−0.4	7.45×10^{-3}	$(2p-)(2p+)^4 12d-J=1$
$2p$-11d	2922.8	2923.2	0.4	9.40×10^{-3}	$(2p-)(2p+)^4 11d-J=1$
$2p$-10d	2941.1	2941.0	−0.1	9.01×10^{-3}	$(2p-)(2p+)^4 10d-J=1$
$2p$-19d		2942.1		1.77×10^{-3}	$(2p-)^2(2p+)^3 19d+J=1$
$2p$-18d	2945.5	2945.4	−0.1	2.53×10^{-3}	$(2p-)^2(2p+)^3 18d+J=1$
$2p$-17d	2949.9	2949.3	−0.6	3.01×10^{-3}	$(2p-)^2(2p+)^3 17d+J=1$
$2p$-16d	2954.4	2953.9	−0.5	3.57×10^{-3}	$(2p-)^2(2p+)^3 16d+J=1$
$2p$-15d	2959.7	2959.6	−0.1	4.57×10^{-3}	$(2p-)^2(2p+)^3 15d+J=1$
$2p$-9d	2966.4	2966.2[a]	−0.2	2.42×10^{-2}	$(2p-)(2p+)^4 9d-J=1$
$2p$-14d	2966.4	2967.0[a]	0.6	7.90×10^{-3}	$(2p-)^2(2p+)^3 14d+J=1$
$2p$-13d	2975.8	2975.6	−0.2	1.19×10^{-2}	$(2p-)^2(2p+)^3 13d+J=1$
$2p$-13s	2977.8	2977.1	−0.7	1.04×10^{-3}	$(2p-)^2(2p+)^3 13s+J=1$
$2s$-6p		2980.2		2.49×10^{-2}	$2s+[2p^6]6p+J=1$
$2s$-6p	2982.3	2982.3	0.0	9.79×10^{-3}	$2s+[2p^6]6p-J=1$
$2p$-12d	2986.4	2986.6	0.2	1.40×10^{-2}	$(2p-)^2(2p+)^3 12d+J=1$
$2p$-11d	3000.7	3000.9[a]	0.0	4.19×10^{-2}	$(2p-)^2(2p+)^3 11d+J=1$
$2p$-8d	3000.7	3001.3[a]	0.4	1.08×10^{-2}	$(2p-)(2p+)^4 8d-J=1$
$2p$-10d	3019.8	3019.4	−0.4	1.56×10^{-2}	$(2p-)^2(2p+)^3 10d+J=1$
$2p$-9d	3045.6	3045.9	0.3	3.44×10^{-2}	$(2p-)^2(2p+)^3 9d+J=1$
$2p$-7d	3054.9	3054.6	−0.3	3.81×10^{-2}	$(2p-)(2p+)^4 7d-J=1$
$2p$-8d	3083.1	3082.7	−0.4	5.11×10^{-2}	$(2p-)^2(2p+)^3 8d+J=1$
$2s$-5p	3127.0	3124.8	−2.2	4.31×10^{-2}	$2s+[2p^6]5p+J=1$
$2s$-5p	3131.7	3129.4	−2.3	1.62×10^{-2}	$2s+[2p^6]5p-J=1$
$2p$-7d	3138.5	3138.4	−0.1	1.13×10^{-1}	$(2p-)^2(2p+)^3 7d+J=1$
$2p$-6d	3141.4	3141.2[b]	−0.2	1.97×10^{-2}	$(2p-)(2p+)^4 6d-J=1$
$2p$-6d	3230.1	3230.6	0.5	1.19×10^{-1}	$(2p-)^2(2p+)^3 6d+J=1$
$2p$-5d	3295.8	3295.5	−0.3	1.11×10^{-1}	$(2p-)(2p+)^4 5d-J=1$
$2p$-5d	3392.0	3391.7	−0.3	2.14×10^{-1}	$(2p-)^2(2p+)^3 5d+J=1$
$2s$-4p	3439.2	3437.7	−1.5	1.09×10^{-1}	$2s+[2p^6]4p+J=1$
$2s$-4p	3450.7	3449.3	−1.4	4.45×10^{-2}	$2s+[2p^6]4p-J=1$
$2p$-4d	3626.1	3626.1	0.0	3.02×10^{-1}	$(2p-)(2p+)^4 4d-J=1$
$2p$-4d	3739.8	3739.8	0.0	5.17×10^{-1}	$(2p-)^2(2p+)^3 4d+J=1$
$2p$-4s	3831.7	3831.6	−0.1	2.40×10^{-2}	$(2p-)^2(2p+)^3 4s+J=1$

[a]The nearness of transition wavelengths makes these transitions unresolvable.

[b]This identification is uncertain because the $2p$-$6d$ transition is quenched through configuration interaction with the $2p^5 7d$ $J=1$ configuration, and is coincidental in wavelength with the Mo^{31+} $2p$-$8d$ transition reported in Table V.

TABLE V. Mo^{31+} ($2p^63s$ ground-state) resonance transitions. The $\Delta\lambda$ values followed by asterisks are found by subtracting the measured transition wavelengths from the value of the oscillator strength weighted average of the calculated transition wavelengths. The column labeled "upper state" shows the $2p$ hole, the spectator electron in braces, and the occupied nd or ns orbital. Note the transitions with the $3p+$ spectator end on the $2p^63pJ=\frac{3}{2}$ level. These lines (3787.4 mÅ) are not true resonance lines since the spectator electron is not in the $3s$ level.

Transition	Obs. λ (mÅ)	Theor. λ (mÅ)	g^*f	$\Delta\lambda$ (mÅ)	Upper state
$2p$-$14d$		2947.4[a]		1.17×10^{-3}	$2p-[3s]14d-J=\frac{1}{2}+$
				1.37×10^{-3}	$2p-[3s]14d-J=\frac{3}{2}$
$2p$-$13d$		2955.5		1.42×10^{-3}	$2p-[3s]13d-J=\frac{1}{2}$
$2p$-$13d$		2957.1		1.06×10^{-3}	$2p-[3s]13d-J=\frac{3}{2}$
$2p$-$12d$		2965.8[a]		1.83×10^{-3}	$2p-[3s]12d-J=\frac{1}{2}+$
				2.09×10^{-3}	$2p-[3s]12d-J=\frac{3}{2}$
$2p$-$11d$		2979.1		2.43×10^{-3}	$2p-[3s]11d-J=\frac{1}{2}$
$2p$-$11d$		2980.7		1.62×10^{-3}	$2p-[3s]11d-J=\frac{3}{2}$
$2p$-$10d$		2996.9[a]		3.37×10^{-3}	$2p-[3s]10d-J=\frac{1}{2}+$
				3.77×10^{-3}	$2p-[3s]10d-J=\frac{3}{2}$
$2p$-$9d$		3021.3[a]		5.11×10^{-3}	$2p-[3s]9d-J=\frac{1}{2}+$
				5.48×10^{-3}	$2p-[3s]9d-J=\frac{3}{2}$
$2s$-$6p$	3027.2	3027.4	0.2	6.58×10^{-3}	$2s+[2p^63s]6p+J=\frac{3}{2}$
$2p$-$14d$		3027.9[a]		2.04×10^{-3}	$2p+[3s]14d+J=\frac{3}{2}+$
				1.96×10^{-3}	$2p+[3s]14d+J=\frac{1}{2}$
$2p$-$13d$		3033.5		2.81×10^{-3}	$2p+[3s]13d+J=\frac{3}{2}$
$2p$-$13d$		3036.4[a]		2.51×10^{-3}	$2p+[3s]13d+J=\frac{1}{2}+$
				2.41×10^{-3}	$2p+[3s]13d+J=\frac{3}{2}$
$2p$-$12d$		3044.3		3.73×10^{-3}	$2p+[3s]12d+J=\frac{3}{2}$
$2p$-$12d$	3047.4	3047.3[a]	-0.1*	3.25×10^{-3}	$2p+[3s]12d+J=\frac{1}{2}+$
				3.06×10^{-3}	$2p+[3s]12d+J=\frac{3}{2}$
$2p$-$8d$		3055.8[a]		1.42×10^{-3}	$2p-[3s]8d-J=\frac{1}{2}+$
				1.78×10^{-2}	$2p-[3s]8d-J=\frac{3}{2}$
$2p$-$11d$		3058.4		5.05×10^{-3}	$2p+[3s]11d+J=\frac{3}{2}$
$2p$-$11d$	3060.1	3060.2[a]	0.1*	4.41×10^{-3}	$2p+[3s]11d+J=\frac{1}{2}+$
				3.97×10^{-3}	$2p+[3s]11d+J=\frac{3}{2}$
$2p$-$10d$		3077.0		7.10×10^{-3}	$2p+[3s]10d+J=\frac{3}{2}$
$2p$-$10d$	3078.9	3078.8[a]	-0.1*	5.50×10^{-3}	$2p+[3s]10d+J=\frac{1}{2}+$
				5.25×10^{-3}	$2p+[3s]10d+J=\frac{3}{2}$
$2p$-$9d$		3102.7		1.05×10^{-2}	$2p+[3s]9d+J=\frac{3}{2}$
$2p$-$9d$	3105.3	3105.7[a]	0.4*	8.07×10^{-3}	$2p+[3s]9d+J=\frac{1}{2}+$
				7.17×10^{-3}	$2p+[3s]9d+J=\frac{3}{2}$
$2p$-$7d$		3108.2[a]		1.10×10^{-2}	$2p-[3s]7d-J=\frac{1}{2}+$
				1.29×10^{-2}	$2p-[3s]7d-J=\frac{3}{2}$
$2p$-$8d$		3138.9		1.61×10^{-2}	$2p+[3s]8d+J=\frac{3}{2}$
$2p$-$8d$	3141.8	3141.9[a]	0.1*	1.21×10^{-2}	$2p+[3s]8d+J=\frac{1}{2}+$
				1.03×10^{-2}	$2p+[3s]8d+J=\frac{3}{2}$
$2s$-$5p$	3172.9	3169.9	-3.0	1.86×10^{-2}	$2s+[2p^63s]5p+J=\frac{3}{2}$
$2p$-$6d$	3192.3	3192.7[a]	0.4*	5.16×10^{-2}	$2p-[3s]6d-J=\frac{1}{2}+$
				3.44×10^{-2}	$2p-[3s]6d-J=\frac{3}{2}$
$2p$-$7d$	3194.3	3194.2	-0.1	2.10×10^{-2}	$2p+[3s]7d+J=\frac{3}{2}$
$2p$-$7d$		3197.2[a]		2.35×10^{-2}	$2p+[3s]7d+J=\frac{1}{2}+$
				2.07×10^{-2}	$2p+[3s]7d+J=\frac{3}{2}$
$2p$-$6d$	3282.8	3283.2	0.5	5.43×10^{-2}	$2p+[3s]6d+J=\frac{3}{2}$
$2p$-$6d$	3285.7	3286.1	0.4	2.66×10^{-2}	$2p+[3s]6d+J=\frac{1}{2}$
$2p$-$6d$		3288.5		3.28×10^{-2}	$2p+[3s]6d+J=\frac{3}{2}$
$2p$-$5d$	3345.1	3344.9[a]	-0.2*	3.55×10^{-2}	$2p-[3s]5d-J=\frac{1}{2}+$

TABLE V. (*Continued*).

Transition	Obs. λ (mÅ)	Theor. λ (mÅ)	g^*f	$\Delta\lambda$ (mÅ)	Upper state
				3.36×10^{-2}	$2p-[3s]5d-J=\frac{3}{2}$
$2p$-$5d$	3442.9	3443.2	0.3	1.15×10^{-1}	$2p+[3s]5d+J=\frac{3}{2}$
$2p$-$5d$	3445.2	3445.4	0.2	5.99×10^{-2}	$2p+[3s]5d+J=\frac{1}{2}$
$2p$-$5d$	3447.8	3447.9	0.1	2.04×10^{-2}	$2p+[3s]5d+J=\frac{3}{2}$
$2s$-$4p$		3474.3		4.13×10^{-2}	$2s+[2p^6 3s]4p+J=\frac{1}{2}$
$2s$-$4p$		3474.6		4.95×10^{-2}	$2s+[2p^6 3s]4p+J=\frac{3}{2}$
$2p$-$4d$	3671.0	3670.3[a]	−0.7	9.38×10^{-2}	$2p-[3s]4d-J=\frac{1}{2}+$
				1.32×10^{-1}	$2p-[3s]4d-J=\frac{3}{2}$
$2p$-$4s$	3759.0	3758.7	−0.3	2.00×10^{-3}	$2p-[3s]4s+J=\frac{3}{2}$
$2p$-$4d$	3785.7	3786.2	0.5	3.07×10^{-1}	$2p+[3s]4d+J=\frac{3}{2}$
$2p$-$4d(3p)+$	3787.4	3787.9[a]	0.5	8.18×10^{-2}	$2p+[3p+]4d+J=\frac{3}{2}+$
				1.19×10^{-1}	$2p+[3p+]4d+J=\frac{1}{2}$
$2p$-$4d$		3789.4		1.51×10^{-1}	$2p+[3s]4d+J=\frac{1}{2}$

[a]These transitions have degenerate upper states and nearly equal oscillator strengths, but they are from configurations which do not mix with each other.

range of the spectrometer system, the $2p_{3/2}$-$4d_{5/2}$ transition in Mo^{32+} at 3739.8 mÅ. The wavelength of this line has been determined by comparison to neighboring lines with accurately known wavelengths, in particular the Lyman-α doublet of Ar^{17+}, nearby satellites, and the $1s^2$-$1s3p$ transition in Cl^{15+} (see Tables I and II). Both Mo^{32+} and Ar^{17+} are located in the plasma center and have the same ion temperature, so the molybdenum line is narrower than the argon lines due to the lower thermal velocity. Similar transitions in sodiumlike Mo^{31+} appear as an unresolved group centered at 3785.7 mÅ. Also apparent is a $2p$-$4d$ transition of magnesiumlike Mo^{30+} at 3715.5 mÅ, although this line is quite weak. Other molybdenum lines in this spectrum are at 3717.8, 3759.1, and 3799.6 mÅ. Shown at the bottom of the figure are computed lines from neonlike, sodiumlike, and magnesiumlike molybdenum, and from hydrogenlike argon and satellites, and heliumlike chlorine. The wavelength agreement of the observed and calculated Mo^{32+} lines is excellent, within 0.5 mÅ for the Mo^{31+} lines and off by 2.9 mÅ for the Mo^{30+} lines.

Figure 2 shows a spectrum from 3.6 to 3.7 Å. Plasma parameters for which this spectrum was obtained were $n_{e0}=1.6\times10^{20}/m^3$ and $T_{e0}=2100$ eV. The strongest line in this spectral region is the $2p_{1/2}$-$4d_{3/2}$ transition of Mo^{32+} at 3626.1 mÅ. Also visible are a pair of unresolved 2p-$4d$ lines of Mo^{31+} at 3670.6 mÅ, and a $2p$-$4d$ line of fluorinelike Mo^{33+} at 3615.3 mÅ. There is also a pair of Mo^{33+} lines around 3604 mÅ, but these blend with the $1s^2$-$1s4p$ transition of Cl^{15+} at 3603.56 mÅ. Shown at the bottom of the figure are theoretical lines from Mo^{32+}, Mo^{31+}, Mo^{33+}, and Cl^{15+}. The wavelength agreement for the neonlike and fluorinelike lines is within 0.2 mÅ. This a particularly interesting portion of the x-ray spectrum since three adjacent charge states are visible simultaneously, and models for ionization state balance

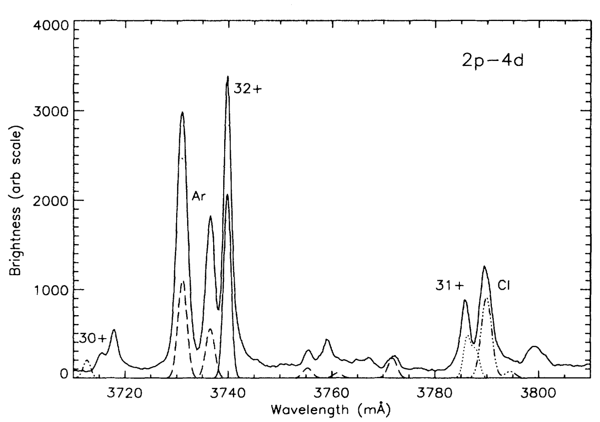

FIG. 1. $2p$-$4d$ transitions in Mo^{32+}, Mo^{31+}, and Mo^{30+}. Theoretical lines for Mo^{32+} (solid), Mo^{31+} (dotted), Mo^{30+} (dash-dot-dash), Ar^{17+} (dashed), and Cl^{15+} (dash-dot-dot-dot-dash) are shown at the bottom.

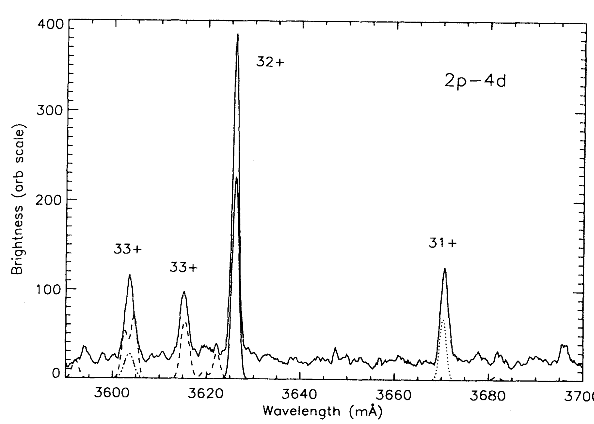

FIG. 2. $2p$-$4d$ transitions in Mo^{32+}, Mo^{31+}, and Mo^{33+}. Theoretical lines for Mo^{32+} (solid), Mo^{31+} (dotted), Mo^{33+} (dashed), and Cl^{15+} (dash-dot-dot-dot-dash) are shown at the bottom.

[25] may be tested. This will be the subject of a forthcoming paper.

In Fig. 3 is shown the spectrum in the vicinity of 3.4 Å, from a discharge with $n_{e0}=1.2\times10^{20}/\mathrm{m}^3$ and $T_{e0}=1500$ eV. The brightest line is the $2p_{3/2}$-$5d_{5/2}$ transition in Mo^{32+} at 3392.0 mÅ, and other $2p$-$5d$ transitions in sodiumlike and magnesiumlike molybdenum are apparent. There are visible two $2s$-$4p$ lines of Mo^{32+} at 3439.2 and 3450.7 mÅ. Also present in this spectrum are Ar^{15+} satellites to the Ar^{16+} $1s^2$-1s3p line with $n=2$ spectators.

TABLE VI. Mo^{33+} ($2s^22p^5$ ground-state) resonance transitions. The column labeled "upper-state" shows the occupancy of the two relativistic $2p$ orbitals and the occupied upper orbital. Transitions labeled with a are to the $2s^22p^5$ $J=\frac{3}{2}$ true ground state; those with b are to the $2s^22p^5$ $J=\frac{1}{2}$ first excited state, and those with c are to the $2s2p^6$ second excited state. Regarding the line at 3267.9 mÅ, see the discussion in the text concerning this identification.

Transition	Obs. λ (mÅ)	Theor. λ (mÅ)	Δλ (mÅ)	g^*f	Upper state
$2p$-$8d$ a		2883.8[a]		4.04×10^{-3}	$(2p-)(2p+)^3(8d-)J=\frac{5}{2}+$
				4.50×10^{-3}	$(2p-)(2p+)^3(8d-)J=\frac{3}{2}$
$2p$-$8d$ a		2883.9		2.90×10^{-3}	$(2p-)(2p+)^3(8d-)J=\frac{1}{2}$
$2p$-$8d$ a		2894.1		4.76×10^{-3}	$(2p-)(2p+)^3(8d-)J=\frac{5}{2}$
$2p$-$7d$ a		2936.1[a]		6.43×10^{-3}	$(2p-)(2p+)^3(7d-)J=\frac{5}{2}+$
				6.09×10^{-3}	$(2p-)(2p+)^3(7d-)J=\frac{3}{2}$
$2p$-$7d$ a		2936.2		4.44×10^{-3}	$(2p-)(2p+)^3(7d-)J=\frac{1}{2}$
$2p$-$7d$ a		2946.7		1.02×10^{-2}	$(2p-)(2p+)^3(7d-)J=\frac{5}{2}$
$2p$-$8d$ a		2967.1		1.38×10^{-1}	$(2p-)^2(2p+)^2(8d+)J=\frac{5}{2}$
$2p$-$6d$ b	3012.6	3013.1	0.5	4.01×10^{-2}	$(2p+)^4(6d-)J=\frac{3}{2}$
$2p$-$6d$ a		3020.5		1.79×10^{-2}	$(2p-)(2p+)^3(6d-)J=\frac{5}{2}$
$2p$-$7d$ a	3022.3	3022.3	0.0	1.82×10^{-2}	$(2p-)^2(2p+)^2(7d+)J=\frac{5}{2}$
$2p$-$7d$ a		3022.5		9.19×10^{-3}	$(2p-)^2(2p+)^2(7d+)J=\frac{3}{2}$
$2p$-$6d$ a		3032.0		1.06×10^{-2}	$(2p-)(2p+)^3(6d-)J=\frac{5}{2}$
$2s$-$5p$ a		3047.1		9.96×10^{-3}	$(2s+)[2p^5](5p+)J=\frac{5}{2}$
$2s$-$5p$ a		3047.5		1.25×10^{-2}	$(2s+)[2p^5](5p+)J=\frac{3}{2}$
$2p$-$6d$ a	3111.6	3111.3	−0.3	3.81×10^{-2}	$(2p-)^2(2p+)^2(6d+)J=\frac{5}{2}$
$2p$-$5d$ a		3172.7		2.38×10^{-2}	$(2p-)(2p+)^3(5d-)J=\frac{5}{2}$
$2p$-$5d$ a		3172.8		2.34×10^{-2}	$(2p-)(2p+)^3(5d-)J=\frac{3}{2}$
$2p$-$5d$ a	3253.4	3252.4	−1.0	3.27×10^{-3}	$(2p-)^2(2p+)^2(5d-)J=\frac{3}{2}$
$2p$-$5d$ b	3261.0	3261.6	0.6	6.48×10^{-2}	$(2p-)(2p+)^3(5d+)J=\frac{1}{2}$
$2s$-$7p$ c	3269.7	3269.8[b]	0.1	3.13×10^{-3}	$(2p-)^2(2p+)^2(7p+)J=\frac{3}{2}+$
					$(2s)[2p^5](5d+)J=\frac{3}{2}$
$2p$-$5d$ a		3271.5		7.09×10^{-2}	$(2p-)^2(2p+)^2(5d+)J=\frac{5}{2}$
$2s$-$4p$ a		3359.0		2.25×10^{-2}	$(2s+)[2p^5](4p+)J=\frac{5}{2}$
$2s$-$4p$ a		3359.7		2.56×10^{-2}	$(2s+)[2p^5](4p+)J=\frac{3}{2}$
$2s$-$4p$ a		3370.6		2.26×10^{-2}	$(2s+)[2p^5](4p-)J=\frac{5}{2}$
$2p$-$4d$ a	3498.0	3497.9	−0.1	7.31×10^{-2}	$(2p-)(2p+)^3(4d-)J=\frac{5}{2}$
$2p$-$4d$ a		3498.3		6.73×10^{-2}	$(2p-)(2p+)^3(4d-)J=\frac{3}{2}$
$2p$-$4d$ a	3513.1	3513.6	0.5	6.45×10^{-2}	$(2p-)(2p+)^3(4d-)J=\frac{5}{2}$
$2p$-$4d$ a	3593.0	3592.1	−0.9	6.69×10^{-2}	$(2p-)^2(2p+)^2(4d+)J=\frac{5}{2}$
$2p$-$4d$ b	3603.2	3602.6	−0.6	1.72×10^{-1}	$(2p-)2p+)^3(4d+)J=\frac{1}{2}$
$2p$-$4d$ b	3604.3	3604.6	0.3	2.32×10^{-1}	$(2p-)(2p+)^3(4d+)J=\frac{3}{2}$
$2p$-$4d$ a	3614.9	3615.1	0.2	1.68×10^{-1}	$(2p-)^2(2p+)^2(4d+)J=\frac{5}{2}$
$2p$-$4d$ a		3616.1		9.87×10^{-2}	$(2p-)^2(2p+)^2(4d+)J=\frac{3}{2}$
$2p$-$4d$ a	3619.8	3619.5	−0.3	2.56×10^{-2}	$(2p-)^2(2p+)^2(4d+)J=\frac{1}{2}$
$2p$-$4d$ b	3622.6	3622.2	−0.4	9.59×10^{-2}	$(2p-)(2p+)^3(4d+)J=\frac{3}{2}$
$2p$-$4s$ b	3682.1	3681.7	−0.4	1.46×10^{-2}	$(2p-)(2p+)^3(4s+)J=\frac{3}{2}$
$2p$-$4s$ a	3696.2	3695.7	−0.5	2.10×10^{-3}	$(2p-)^2(2p+)^2(4s+)J=\frac{5}{2}$
$2p$-$4d$ b	3717.8	3715.5	−2.3	9.18×10^{-2}	$(2p-)^2(2p+)^2(4d-)J=\frac{3}{2}$

[a]These transitions have degenerate upper states and nearly equal oscillator strengths, but they are from configurations that do not mix with each other.
[b]Transition is allowed only through configuration mixing.

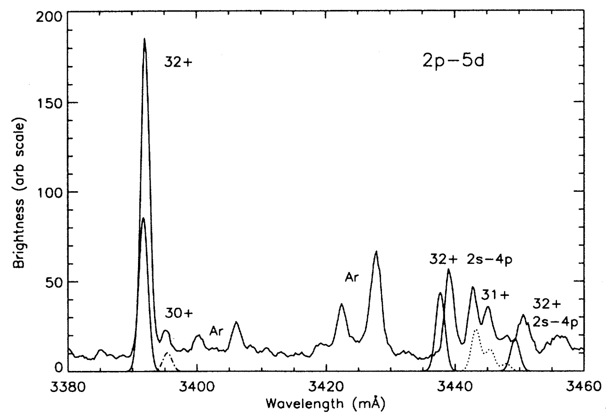

FIG. 3. $2p$-$5d$ transitions in Mo^{32+} (solid), Mo^{31+} (dotted), and Mo^{30+} (dash-dot-dash), and $2s$-$4p$ transitions in Mo^{32+} (solid).

The wavelength agreement is good (within 0.3 mÅ) for transitions with a $2p$ lower level, but those with the $2s$ lower level are off by 1.5 mÅ. The $2s2p^64p$ $J=1$ levels are well separated in energy from the levels of other configurations with the same parity, so their wave functions are extremely pure. The accuracy of calculated transition wavelengths for radiative decays to an inner-shell hole is known to be worse than that for decays to a valence hole; indeed, for neonlike charge states of heavier elements, observations [26] have shown that calculations consistently overestimate the self-energy contribution of the $2s$ hole to the $2s$-np transitions. This may be due to the fact that the calculations of the Lamb shift and the Breit interaction energy in RELAC are approximate (a discussion of their associated contributions to uncertainties in transition wavelengths can be found in Ref. [22]).

The spectrum between 3.0 and 3.1 Å is shown in Fig. 4. This was obtained from a series of several similar discharges with $n_{e0}=1.3\times10^{20}/\mathrm{m}^3$ and $T_{e0}=1600$ eV. The Mo^{32+} series $2p_{3/2}$-$nd_{5/2}$ with $n=8$, 9, 10, 11, and 12 can be seen, as well as the $2p_{1/2}$-$7d_{3/2}$ (3054.9 mÅ) and $2p_{1/2}$-$8d_{3/2}$ (unresolved from $2p_{3/2}$-$11d_{5/2}$) transitions. Theoretical lines (solid) are shown at the bottom of the figure, and the wavelength agreement is excellent.

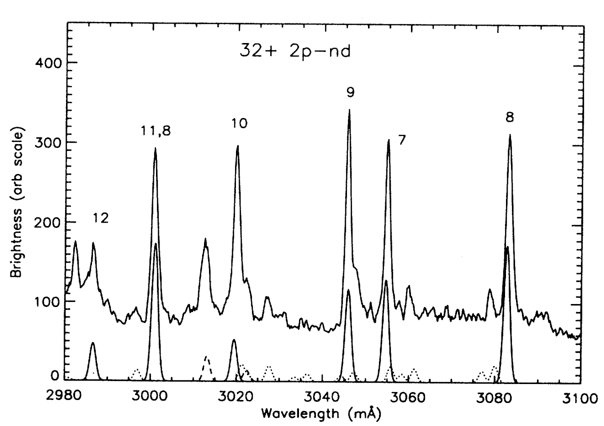

FIG. 4. $2p_{3/2}$-$nd_{5/2}$ transitions with $8\le n\le13$ in Mo^{32+}. Theoretical lines for Mo^{32+} (solid), Mo^{31+} (dotted), and Mo^{33+} (dashed) are shown at the bottom.

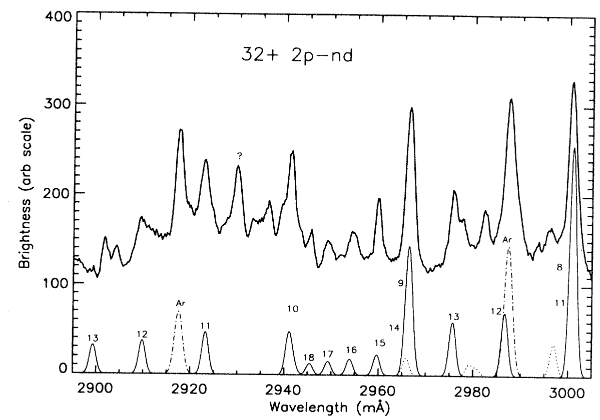

FIG. 5. Transitions in Mo^{32+} near the $2p_{3/2}$-$nd_{5/2}$ series limit, including the $2p_{1/2}$-$nd_{3/2}$ series with $8\le n\le13$ and the $2p_{3/2}$-$nd_{5/2}$ series with $11\le n\le18$. Theoretical lines for Mo^{32+} (solid), Mo^{31+} (dotted), and Ar^{17+} (dash-dot) are shown at the bottom.

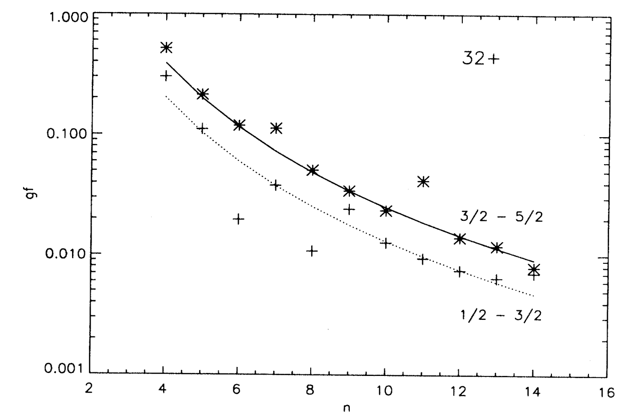

FIG. 6. gf values for $2p_{3/2}$-$nd_{5/2}$ (asterisks) and $2p_{1/2}$-$nd_{3/2}$ (plus signs) transitions in Mo^{32+} as a function of upper level principal quantum number n. Curves are proportional to n^{-3}.

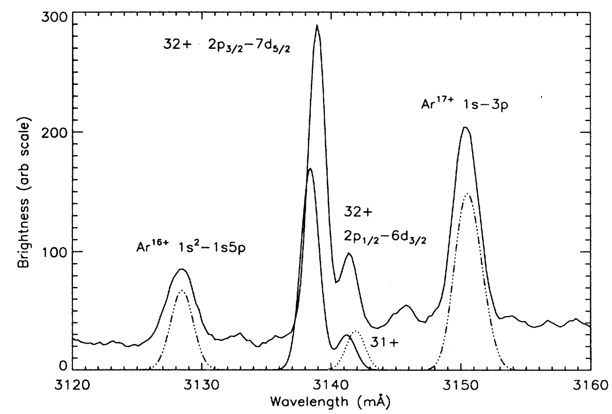

FIG. 7. $2p_{3/2}$-$7d_{5/2}$ transition in Mo^{32+}. Theoretical lines for Mo^{32+} (solid), Mo^{31+} (dotted), Ar^{16+}, and Ar^{17+} (dash-dot-dot-dot-dash) are shown at the bottom.

TABLE VII. Mo^{30+} ($2p^6 3s^2$ ground state) resonance transitions. The column labeled "upper state" shows the $2p$ hole, the spectator electrons in braces, and the occupied nd or ns orbital.

Transition	Obs. λ (mÅ)	Theor. λ (mÅ)	Δλ(mÅ)	g^*f	Upper state
$2p$-$14d$		3005.3		3.51×10^{-3}	$2p-[3s^2]14d-J=1$
$2p$-$13d$		3013.2		4.22×10^{-3}	$2p-[3s^2]13d-J=1$
$2p$-$12d$		3023.3		5.39×10^{-3}	$2p-[3s^2]12d-J=1$
$2p$-$11d$		3036.4		7.12×10^{-3}	$2p-[3s^2]11d-J=1$
$2p$-$10d$		3053.8		9.77×10^{-3}	$2p-[3s^2]10d-J=1$
$2p$-$9d$		3077.7		1.43×10^{-2}	$2p-[3s^2]9d-J=1$
$2p$-$14d$		3087.1		6.45×10^{-3}	$2p+[3s^2]14d+J=1$
$2p$-$13d$		3095.5		8.14×10^{-3}	$2p+[3s^2]13d+J=1$
$2p$-$12d$		3106.0		1.11×10^{-2}	$2p+[3s^2]12d+J=1$
$2p$-$8d$	3112.8	3111.9	−0.9	3.05×10^{-2}	$2p-[3s^2]8d-J=1$
$2p$-$11d$	3118.1	3119.6	1.5	1.28×10^{-2}	$2p+[3s^2]11d+J=1$
$2p$-$10d$		3138.1		1.78×10^{-2}	$2p+[3s^2]10d+J=1$
$2p$-$7d$		3160.4		5.91×10^{-2}	$2p-[3s^2]7d-J=1$
$2p$-$9d$		3161.8[a]		5.31×10^{-5}	$2p+[3s^2]9d+J=1$
$2p$-$8d$	3201.3	3199.4	−1.9	3.78×10^{-2}	$2p+[3s^2]8d+J=1$
$2s$-$5p$	3211.8	3210.9	−0.9	3.74×10^{-2}	$2s+[2p^6 3s^2]5p+J=1$
$2p$-$6d$	3246.2	3243.2	−3.1	6.85×10^{-2}	$2p-[3s^2]6d-J=1$
$2p$-$7d$	3253.2	3250.4	−2.8	5.00×10^{-2}	$2p+[3s^2]7d+J=1$
$2p$-$6d$	3339.6	3337.5	−1.9	1.10×10^{-1}	$2p+[3s^2]6d+J=1$
$2p$-$5d$	3395.1	3395.4	0.3	1.03×10^{-1}	$2p-[3s^2]5d-J=1$
$2p$-$5d$	3497.0	3497.1	0.1	1.93×10^{-1}	$2p+[3s^2]5d+J=1$
$2s$-$4p$		3507.2		1.11×10^{-1}	$2s+[2p^6 3s^2]4p+J=1$
$2p$-$4d$	3715.5	3712.6	−2.9	2.86×10^{-1}	$2p-[3s^2]4d-J=1$
$2p$-$4s$	3799.6	3800.1	0.5	2.67×10^{-3}	$2p-[3s^2]4s+J=1$
$2p$-$4d$	3834.8	3831.6	−3.2	5.03×10^{-1}	$2p+[3s^2]4d+J=1$

[a]This transition is quenched through configuration interaction with the $2p^5 3s^2 7d$ configuration.

Wavelength calibration was obtained by comparison to nearby Ar^{16+} ($1s^2$-$1snp$ with $5\le n\le 13$) lines [20,27] (see Table I). Mo^{31+} (dotted) and Mo^{33+} (dashed) lines are also identified.

Shown in Fig. 5 is a spectrum from 2.9 to 3.0 Å, obtained from a series of identical discharges with $n_{e0}=1.7\times10^{20}/m^3$ and $T_{e0}=2300$ eV. The $2p_{3/2}$-$nd_{5/2}$ series up to $n=18$ and the $2p_{1/2}$-$nd_{3/2}$ series with $8\le n\le 12$ are clearly resolvable. Above $n=18$, the lines of the $2p_{3/2}$-$nd_{5/2}$ series blend together, up to the series limit at 2914.78 mÅ. Also shown are two Ar^{17+} lines used for the wavelength calibration, and an unidentified molybdenum line at 2929.9 mÅ. At the bottom of the figure are calculated lines from Mo^{32+} (solid), Mo^{31+} (dotted), and Ar^{17+} (dot-dash).

The results, experimental, theoretical, and their comparisons, are summarized in Tables IV–VII for the charge states Mo^{30+}–Mo^{33+}. Wavelength agreement is better than 0.5 mÅ in most cases. In Figs. 1–5, the relative intensities of the theoretical lines from a given charge state are determined by the gf values from the tables.

The gf values from the $2p_{3/2}$-$nd_{5/2}$ and $2p_{1/2}$-$nd_{3/2}$ series in Mo^{32+} are plotted as a function of n in Fig. 6. Also shown are curves proportional to n^{-3} (the dependence for H-like ions at high n), which reflect the general trend. The $2p_{1/2}$-$6d_{3/2}$ transition, however, is about a factor of 3 below this trend and the $2p_{3/2}$-$7d_{5/2}$ transition is nearly a factor of 2 above the trend. This is supported by the observed line intensities. Shown in Fig. 7 is a spectrum that includes the Mo^{32+} $2p_{3/2}$-$7d_{5/2}$ transition at 3138.5 mÅ, as well as the Ar^{16+} $1s^2$-$1s5p$ and Ar^{17+} $1s$-$3p$ lines used for the wavelength calibration (see Table I). There is also a feature at 3141.8 mÅ, which is a blend of the Mo^{32+} $2p_{1/2}$-$6d_{3/2}$ line (solid) and a $Mo^{31+}$$2p$-$8d$ line (dotted). The ratio of the two calculated Mo^{32+} gf values is 5.7, whereas the ratio from the two curves in Fig. 6 for these lines is 1.2. From Fig. 7 it is clear that the $2p_{3/2}$-$7d_{5/2}$ line is much stronger (a factor of 4.3) than the $2p_{1/2}$-$6d_{3/2}$ line, consistent with the calculated gf values. The reason that the $2p_{1/2}$-$6d_{3/2}$ line is so weak is because of the configuration interaction between the $(2p^5)_{1/2}6d_{3/2}$ $J=1$ state and the $(2p^5)_{3/2}7d_{j'}$ $J=1$ states that occurs due to their near degeneracy in energy. Similar effects have been observed and modeled in other tokamak plasmas [28]. The same effect is seen on the $2p_{1/2}$-$8d_{3/2}$ gf value in Fig. 6; this value is also below the smooth curve. The $(2p^5)_{1/2}$-$8d_{3/2}$ $J=1$ level interacts with the nearby $(2p^5)_{3/2}$-$11d_{j'}$ $J=1$ levels. However, it is unresolved from the $2p_{3/2}$-$11d_{5/2}$ transition, so their relative intensities cannot be determined (see Fig. 4). Additional degeneracies exist between the $2p_{1/2}$-$9d_{3/2}$ and $2p_{3/2}$-$14d_{5/2}$ levels (see Fig. 5).

CONCLUSIONS

X-ray spectra of highly ionized molybdenum in the wavelength range from 2.90–3.84 Å have been obtained from the Alcator C-Mod tokamak. Wavelengths for $2p$-nd transitions with $n \geq 4$ for neonlike, sodiumlike, magnesiumlike, and fluorinelike molybdenum have been determined by reference to nearby argon and chlorine lines, with an accuracy of ± 0.1 mÅ. Line identifications have been made by comparison to atomic structure calculations, using a fully relativistic, parametric potential code. The agreement between measured and theoretical wavelengths is quite good, with most lines within 0.5 mÅ. Configuration interaction has been seen to affect the intensities of transitions with nearly degenerate upper states.

ACKNOWLEDGMENTS

The authors would like to thank K. Giesing for assistance with the data reduction, T. Luke for electron density measurements, A. Hubbard for electron temperature measurements, and the Alcator C-Mod operations group for expert running of the tokamak. Work supported at MIT by U.S. DOE Contract No. DE-AC02-78ET51013 and at LLNL by U.S. DOE Contract No. W-7405-ENG-48.

[1] R. C. Isler, Nucl. Fusion **24**, 1599 (1984).
[2] C. DeMichelis and M. Mattioli, Rep. Prog. Phys. **47**, 1233 (1984).
[3] G. M. Zeng *et al.*., J. Appl. Phys. **72**, 3355 (1992).
[4] A. Wouters *et al.*, J. Opt. Soc. Am. B **5**, 1520 (1988).
[5] C. Jupen *et al.*, Phys. Scr. **41**, 669 (1990).
[6] B. K. F. Young *et al.*, Phys. Rev. A **62**, 1266 (1989).
[7] V. A. Boiko *et al.*, J. Phys. B **11**, 503 (1978).
[8] A. L. Gogava *et al.*, Opt. Spektrosk. **64**, 726 (1988) [Opt. Spectrosc. (USSR) **64**, 435 (1988)].
[9] Y. K. Kim *et al.*, Phys. Rev. A **44**, 148 (1991).
[10] I. H. Hutchinson *et al.*, Phys. Plasmas **1**, 1511 (1994).
[11] F. Wagner and K. Lackner in *Physics of Plasma Wall Interactions in Controlled Fusion,* Vol. 131 of NATO Advanced Study Institute; Series B: Physics, edited by D. E. Post and R. Behrisch (Plenum, New York, 1986), p. 931.
[12] J. E. Rice *et al.*, Phys. Rev. A **22**, 310 (1980).
[13] E. Källne, J. Källne, and R. D. Cowan, Phys. Rev. A **27**, 2682 (1983).
[14] P. Burkhalter *et al.*, Phys. Rev. A **18**, 718 (1978).
[15] J. E. Rice and E. S. Marmar, Rev. Sci. Instrum. **61**, 2753 (1990).
[16] E. S. Marmar *et al.*, Phys. Rev. A **33**, 774 (1986).
[17] G. W. Erickson, J. Phys. Chem. Ref. Data **6**, 831 (1977).
[18] V. A. Boiko *et al.*, J. Phys. B **10**, 3387 (1977).
[19] L. A. Vainshtein and U. I. Safronova, Phys. Scr. **31**, 519 (1985).
[20] J. F. Seely and U. Feldman, Phys. Rev. Lett. **54**, 1016 (1985).
[21] M. Klapisch, Comput. Phys. Commun. **2**, 269 (1971).
[22] M. Klapisch, J. L. Schwob, B. S. Fraenkel, and J. Oreg, J. Opt. Soc. Am. **67**, 148 (1977).
[23] A. Bar-Shalom and M. Klapisch, Comput. Phys. Commun. **50**, 375 (1988).
[24] R. D. Cowan, *The Theory of Atomic Structure and Spectra* (University of California Press, Berkeley, 1981), pp. 433 and 434.
[25] K. Fournier *et al.*, Bull. Am. Phys. Soc. **39**, 1765 (1994).
[26] P. Beiersdorfer, M. H. Chen, R. E. Marrs, and M. Levine, Phys. Rev. A **41**, 3453 (1990).
[27] J. E. Rice, E. S. Marmar, E. Källne, and J. Källne, Phys. Rev. A **35**, 3033 (1987).
[28] M. Finkenthal *et al.*, Phys. Rev. A **39**, 3717 (1989).